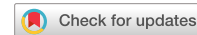


communications materials

ARTICLE



<https://doi.org/10.1038/s43246-021-00190-7>

OPEN

Mechanical origin of martensite-like structures in two-dimensional ReS₂

Lingli Huang ^{1,2,6}, Fangyuan Zheng ^{3,4,6}, Honglin Chen ^{1,6}, Quoc Huy Thi ^{1,2}, Xin Chen ¹, Haijun Liu ¹, Chun-Sing Lee¹, Qingming Deng ^{5✉}, Jiong Zhao ^{3,4✉} & Thuc Hue Ly ^{1,2✉}

Martensite is a needle-shaped microstructure formed by a rapid, diffusionless transformation and significantly affects the mechanical properties of materials. Here, in two-dimensional ReS₂ we show that martensite-like domain structures can form via a diffusionless transformation, involving small lattice deformations. By analyzing the strain distribution and topology of the as-grown chemical vapor deposition samples, we find that cooling-induced strain at the ReS₂/substrate interface is responsible for the mechanical loading and is essential for martensite-like domain formation. Meanwhile, the effect of cooling rate, flake size and substrate on the microstructures revealed the mechanical origin of the transformation. The strain-induced lattice reconstructions are rationalized and possibly lead to ferroelastic effects. In view of the strong anisotropy in electronic and optical properties in two dimensional materials like ReS₂, opportunities exist for strain-correlated micro/nanostructure engineering, which has potential use in next-generation strain-tunable devices.

¹ Department of Chemistry and Center of Super-Diamond & Advanced Films (COSDAF), City University of Hong Kong, Kowloon, Hong Kong, China. ² City University of Hong Kong Shenzhen Research Institute, Shenzhen, China. ³ Department of Applied Physics, The Hong Kong Polytechnic University, Kowloon, Hong Kong, China. ⁴ The Hong Kong Polytechnic University Shenzhen Research Institute, Shenzhen, China. ⁵ Physics Department and Jiangsu Key Laboratory for Chemistry of Low-Dimensional Materials, Huaiyin Normal University, Huai'an, China. ⁶These authors contributed equally: Lingli Huang, Fangyuan Zheng, Honglin Chen. ✉email: q.deng@hytc.edu.cn; jiong.zhao@polyu.edu.hk; thuchly@cityu.edu.hk

Two-dimensional (2D) materials are attractive to the community for their unprecedented deformability and a variety of novel properties^{1–4}. Similar to the bulk semiconductors, extensive efforts have been devoted to the strain engineering on 2D materials^{5,6}. Including graphene and transition metal dichalcogenides (TMDs), the electronic band structures of 2D materials are prevalently sensitive to the external loading, leading to significant changes in electrical or optical properties^{7–9}. It is more intriguing for the anisotropic 2D materials such as rhenium disulfide (ReS_2), as the crystal lattice reconstructions and sub-domain structures can contribute an additional degree of freedom for control^{10–12}.

According to the elasticity and plastic theory, stressing the three-dimensional (3D) bulk materials can result in a certain deformation in crystal lattices¹³. On the contrary, for 2D materials, which can be regarded as nearly ideal plane-stress deformation due to the vanishing thickness^{14,15}, the induced strain could have higher uncertainties. For example, the out-of-plane undulation/rippling in 2D materials is almost unavoidable, especially under compressive or shear stress¹⁶. Such rippling is also intrinsic to stabilize the suspended 2D crystals¹⁷. On the other hand, 2D materials can usually be stressed close to the ideal strength due to the exclusion of atomic defects¹⁸, leaving the elasticity entering the deep nonlinear regime¹⁹. Indeed, abundant theories and experiments on the 2D materials such as graphene and 2D TMDs have shown their excellent mechanical properties, which also justify their great potentials in future applications^{20–25}.

Compared to the isotropic 2D counterparts, less is known about the anisotropic 2D materials. It has been reported the 2D ReS_2 or ReSe_2 can undergo atomic lattice reconstruction under electron beam effect²⁶. The 2D ReS_2 after growth were also observed with stripe-like or needle-like domains and parallel domain boundaries, though the as-grown samples on the growing substrates without transfer have not been systematically investigated^{27,28}. Apart from that, the anisotropic atomic structures (viz. the directional Re atomic chains, see Fig. 1a) in these T' phases of 2D TMDs have also been manifested to have anisotropic electrical and optical properties^{22,28–34}. The anisotropic

high electron mobility and the hierarchical domain structure in ReS_2 may create new possibilities for the property modulation in 2D structures.

It was explained that the sub-domain structures in 2D ReS_2 exist with mirror (twin) boundaries^{27,34}. However, the origin of these domains is not clear yet. As we will discuss in the current paper, the rich-domain structures in 2D ReS_2 can be attributed to the atomic lattice reorganization under ultra-low strain. Here we will give a complete explanation for the origin of all the needle-like domain patterns with a complete list of domain boundary types. These observed domains are not originated during growth in the chemical vapor deposition (CVD) at high temperature (CVD-grown products are virtually single crystal for each flake from a single nuclei), rather they are attributed to the cool-down stress by sample-substrate thermal expansion differences. The rich-domain structures in 2D ReS_2 are formed by lattice reorganization during the cooling process, which resembles the formation of the needle-like microstructure of martensite by iron atomic rearrangement during the cooling process^{35,36}. Here the origin of “martensite-like” structures in anisotropic 2D ReS_2 is investigated.

Results and discussion

The martensite-like domain structures in 2D ReS_2 . The monolayer and multilayer 2D ReS_2 samples in our experiments were synthesized either by the CVD method or mechanical exfoliation method (see “Methods” section)^{37,38}. Similar to previous reports, the CVD-grown monolayer (1L) ReS_2 samples, irrespective of monolayer or multilayers, predominantly exhibited sub-domain structures and parallel stripe patterns under polarized optical microscopy (OM) (Fig. 1a). After the samples were wet-transferred (see “Methods” section) onto new substrates, the domain and stripe patterns persisted (Supplementary Fig. 1). Comparatively, the mechanical exfoliated 1L- ReS_2 samples did not show any domain patterns above (Fig. 1b). We have verified the above patterns using dynamic force microscopy on the as-grown samples (DFM, see “Methods” section), in the topography

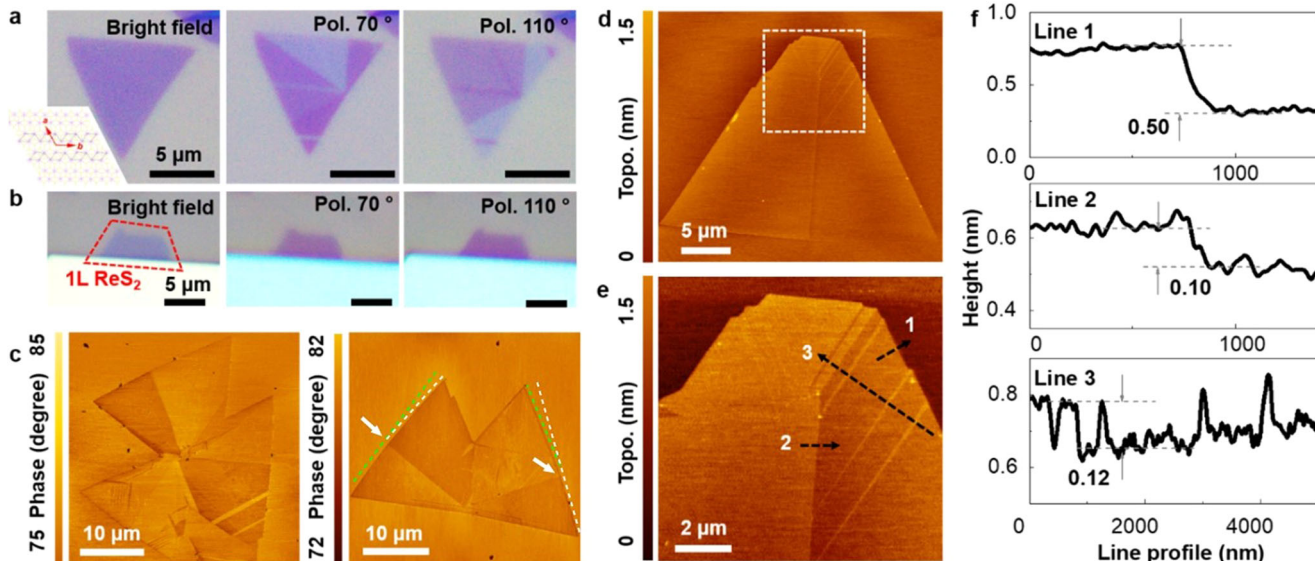


Fig. 1 The martensite-like domain structures in 2D ReS_2 . **a, b** The color optical images under bright field, polarized 70° and 110° for CVD-grown 1L- ReS_2 transferred on 300 nm SiO_2/Si substrate, and mechanical exfoliated ReS_2 on 300 nm SiO_2/Si substrate, respectively. The inset shows the crystal structure model of monolayer (1L) ReS_2 with chain-like structures (dashed black lines). **c, d** The DFM phase and topography images of monolayer ReS_2 as grown on mica (ReS_2/mica). **e** The magnified DFM topography image corresponding to the white dashed square in **d**. **f** The line profiles corresponding to the black dashed lines in **e**.

images, the similar patterns can be clearly identified, while the phase images can further enhance the domain contrasts (Fig. 1c, the corresponding topography images show in Supplementary Fig. 2). Notably, the multilayer ReS_2 also possess similar sub-domain structures irrespective of the thickness (Supplementary Fig. 3). These domain structures should be attributed to the different orientated crystal grains of 2D ReS_2 . Hence the DFM phase images can be understood—domain contrast came from the different molecular interactions between scanning tips and ReS_2 surfaces along different crystal orientations. However, the brighter contrast half (higher) in the DFM topography image implies there is partial delamination between the 2D flake and substrate (Fig. 1d-f). Particularly, for the triangle flakes, the needle-like or stripe-like patterns are more likely to form in the undelaminated half flakes (the darker halves in the DFM topography images) than the delaminated half (the brighter halves in DFM topography images) (Fig. 1e), which will be explained later.

The strain distribution of the as-grown ReS_2 . Here we used the angle-resolved polarized Raman (ARPR) spectroscopy³⁹ to examine the 2D monolayer ReS_2 samples without transfer (which means they are measured on the growth substrates directly). The polarized optics in our Raman setup has been verified on 1L- MoS_2 prior to the measurement on ReS_2 (Supplementary Figs. 4 and 5). We have correlated the Raman and DFM results for the same ReS_2 flakes (CVD grown on fluorophlogopite mica) (see “Methods” section). Considering the anisotropic optical property of ReS_2 and the non-polarized Raman measurement is less sensitive to anisotropic structures, the ARPR measurement is imperative for the in-plane anisotropic ReS_2 (Fig. 2). In the DFM phase images, the brighter color contrast indicates the lattice reconstruction area and the darker color contrast indicates the delaminated area (Fig. 2a). The Raman peak at 3, 4, 5, and 6 (Fig. 2b) are the Re atoms in-plane vibration modes⁴⁰. Different vibration modes in 1L- ReS_2 are excited with different polarization directions. Besides, the ARPR intensity of peak 5 indicates the orientation of Re chain³⁴. As shown in Fig. 2c, d, the intensities of Raman peak 5 exhibit stark differences between the delaminated/undelaminated domains. The Raman intensity variance can be explained by the different strain levels. The crystal orientations influence the angle of reaching maximum peak intensity (Fig. 2e, f). Peaks 3, 5, and 6 of sub-domain I reach maximum intensity at polarized angles 138°, 70°, and 65° (Fig. 2e). It shows a decreasing trend. On the contrary, the peaks 3, 5, and 6 of sub-domain II reach the maximum intensity at polarized angles 108°, 135°, and 150° (Fig. 2f). It shows an increasing trend. The inverse trend indicates the different lattice orientations (Fig. 2e, f). However, as for the orientation of each vibration mode, there are still huge intensity differences. As shown in Fig. 2g-i, the maximum peak intensity at peaks 3, 5, and 6 of sub-domain I are ~120, ~250, and ~250% of sub-domain II. The lattice reconstructed area has stronger APRP intensity than the delaminated area. The reduction of Raman intensity of ReS_2 is owing to the existed strain⁴¹. Hence, the residual strain effects are verified by the difference of ARPR intensity at oriented directions. More strain is released in the lattice reconstructed area, leading to a higher ARPR intensity than the delaminated area.

Cooling-induced train at ReS_2 /substrate interface. The delamination of CVD as-grown flakes usually occurs during the cooling down process, so that the cooling rate is modulated to investigate the cool-down stress (Fig. 3). The slow-cooling rate produces less domain patterns on the sample (Fig. 3a, d), while the fast-cooling rate leads to more and denser domain patterns on 1L- ReS_2 sample (Fig. 3c, f). Initially, the sub-domain structures

observed under polarized 70° OM images (Fig. 3a-c) indicate the distinguishing Re chain orientations. Furthermore, the needle-like patterns are studied using the DFM topography and phase characterizations (Fig. 3d-f). The delaminated areas have brighter contrast (higher) in DFM topography images resulted from the release of the cool-down stress. On the other hand, the lattice reconstruction is the stress release of the undelaminated area. Apparently shown in DFM phase images, the delaminated area shows the darker contrast and the lattice reconstructed area shows the brighter contrast. With a slow-cooling rate, the interfacial stress can be released by a large area, continuous flake-substrate delamination, while with a fast-cooling rate, the interfacial stress tends to be released through local lattice reconstructions. Fast cooling exerts larger cooling stress due to less strain relaxation, providing larger tensile stress on the 1L- ReS_2 . As a result, the fast-cooling ReS_2 flakes have more needle-like patterns.

The residual stress/strain is distinctly different in the original lattice (delaminated) and lattice reconstructed domains. More strain is released in the lattice reconstructed areas (Fig. 2), leading to lowered remaining stress in those areas. According to the DFM topography results, the magnitude of the partial delaminations in lattice reconstructed domains is within 0.1–0.2 nm. With delaminations, the lattice mismatch strains between ReS_2 and substrate upon cooling are released. According to the Poisson ratio effect (elasticity of membranes), if the tensile strain in the membrane is relaxed, the thickness of the membrane will increase, in agreement with our DFM results as well. On the other hand, it is intrinsic behavior for the different optical responses under polarized light along with the different lattice directions (or domains) in 2D ReS_2 ²⁷. However, in our experiments, the contrast of ARPR spectroscopy and DFM topography results between different domains should be attributed to the contrasted residual strain levels in the pristine and reconstructed domains.

The strain-originated domain structure can also explain the absence of domain patterns in the mechanical exfoliated ReS_2 flakes. The mechanical exfoliated flakes mainly experienced out-of-plane stressing instead of in-plane stress which might induce domain structures. Except for the out-of-plane bending, no apparent in-plane straining that is required for mechanical twinning is applied during the mechanical exfoliation process⁴². In CVD-grown flakes, owing to the easier relief of interfacial stress in smaller flakes and larger residual stress remained in larger flakes, the smaller 1L- ReS_2 flakes usually possess remarkably less domain structures (Fig. 4a-f). It is also found enhanced/increased domain structures in 1L- ReS_2 grown on SiO_2/Si substrate, compared with fluorophlogopite mica and c-face sapphire. It is attributed to the larger thermal expansion coefficient (TEC) misfits of SiO_2/Si with 2D anisotropic materials (Fig. 4g-o and Supplementary Table 1). The substrates with lower TEC such as Si/SiO_2 will shrink much less than 1L- ReS_2 during cooling, hence induce a larger traction force. The CVD-grown ReS_2 samples after transfer onto another substrate (Supplementary Fig. 1) kept the original patterns after synthesis due to no additional loading is applied in the processing. For the multilayer specimens, the cooling down strain can be actually transferred by interlayer interactions (signature of T' phases of TMD materials)⁴³, inducing similar lattice switching behavior throughout all the thicknesses.

The sub-domains boundaries trigger by the above lattice reconstructions have been fully corroborated by our high-resolution scanning transition electron microscopy (STEM) observations (Fig. 5a-c and Supplementary Fig. 6), which should be nucleated from the free edges (lowest strain energy cost at the edges). In the case of CVD cooling down the process for 2D ReS_2 in our experiments, the biaxial thermal expansion difference

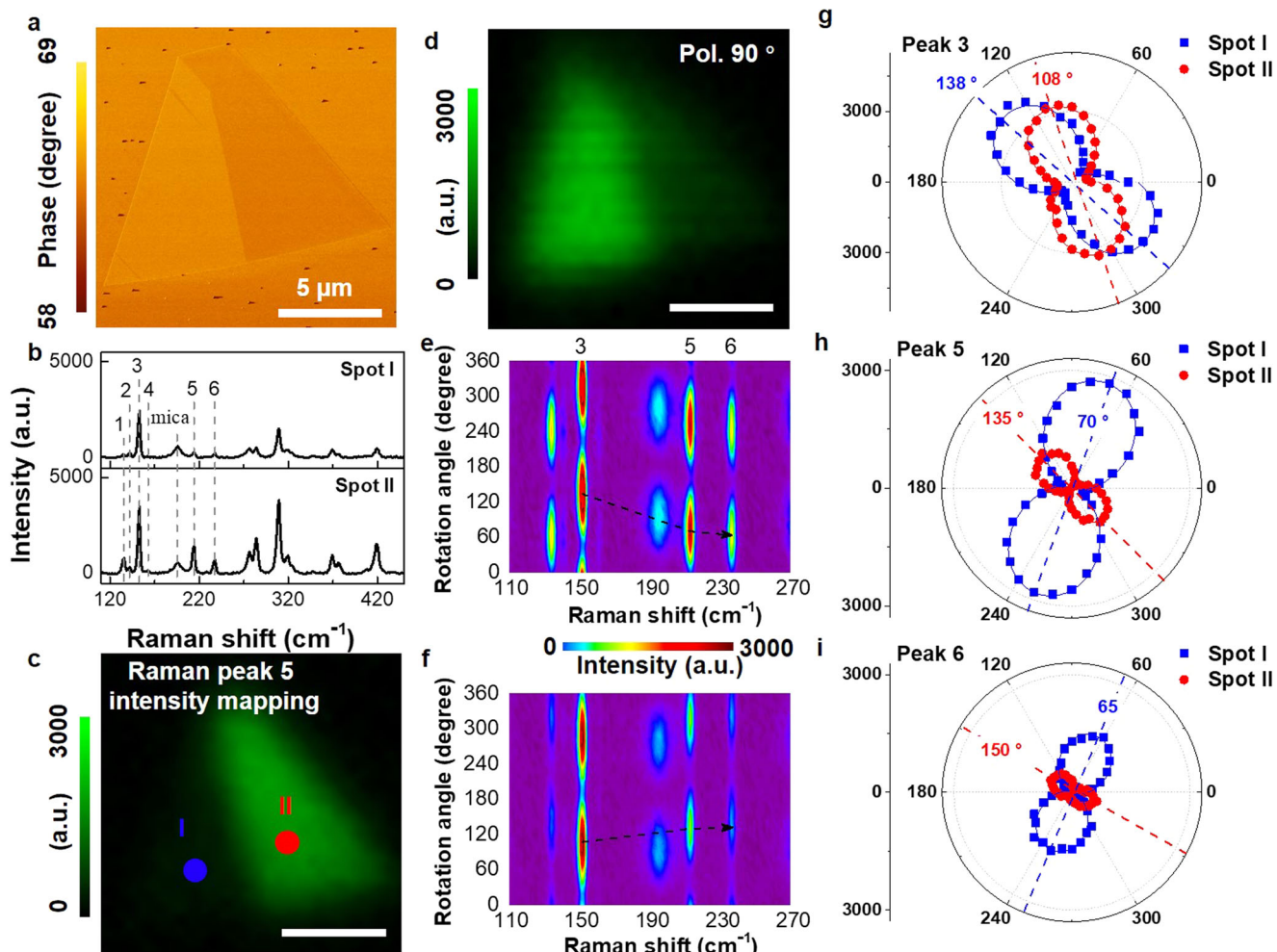


Fig. 2 The ARPR characterizations on CVD-grown 2D 1L-ReS₂. **a** The DFM phase image. **b** The single Raman spectra (polarized 0°) of 1L-ReS₂ at different sub-domains corresponding to the blue and red spots in **c**. **c**, **d** The polarized 0° and polarized 90° Raman peak 5 intensity mapping, respectively. **e**, **f** Polarization-dependent Raman intensity mappings corresponding to the blue and red spots in **c**, respectively. **g–i** Angle-dependent polar plots for sub-domain I and sub-domain II at peaks 3, 5, 6 (scatter) and fitted by Sine function (line), respectively.

between ReS₂ and underlying substrates (mica or sapphire) created a tensile strain field in ReS₂. There are no clear boundary conditions for strain/stress, the ReS₂ flakes and substrates are engaged by the vdW interactions (can be rationalized as static frictions) at the interface. In contrast to the out-of-plane buckling under compressive cooling down strains in 2D WS₂⁴⁴, the interactions between ReS₂ and substrates here can create the homogeneous in-plane tensile strain in 2D ReS₂, while the relative sliding and delamination between 2D flakes and the substrates prefer to start at the free edges (Fig. 5d, e). Assuming the frictional force (between ReS₂ and substrate) is constant (maintained at maximum) in final states near edges at room temperature, the tensile stress/strain can be assigned according to the location in the 2D flakes (Fig. 5f, g). Apparently, the normal stress pointing to the edges will decrease from the corners to the interiors along edges, causing the shear strain in the “wing” like structures. Therefore, the energy favorable twinning domains will be triggered from the corners, sweep over half of the edges, and be ceased at the middle points of edges, as we observed above. The delaminated half (brighter half in the DFM topography images, e.g., Fig. 1d-f) thus have less or even no sub-domain structures due to the relief of interfacial stress upon this first-step delamination, while the undelaminated half (darker half in the DFM topography images) will undergo further

transformations by the tensile stress starting from the edges, forming the needle-like sub-domains in the darker half.

The lattice reconstructed domains thus can have stark differences in residual stress, especially between sample and substrates. Compared to the original lattice domains (delaminated sub-domains), the interfacial strains have been largely released during lattice reconstructions in reconstructed domains. The contrasts between original and reconstructed domains seen by the DFM topography images (Fig. 1e) and the polarized optical characterizations (Fig. 2b-i) can be attributed to the strain differences between reconstructed and pristine domains. Particularly, the small shear angle changes in lattice directions, for pristine and reconstructed domains, can also be clearly visualized on free edges in the DFM/optical images (Fig. 1a, c, d and 3). The tensile traction exerted on the monolayer ReS₂ samples will cause the stripe patterns along certain crystal directions (Figs. 1e and 4). Since all of the twin boundaries shown in Fig. 6 have very low lattice mismatches thus low formation energies, in real samples we can find quite complicated domain structures consisting of all the possible domain boundaries, crossing with angles close to 30°, 60°, 90°, 120°, and 150° (Supplementary Fig. 7).

The structural and strain analysis of twin structures by lattice reconstructions in 1L-ReS₂. 2D ReS₂ has a monoclinic crystal

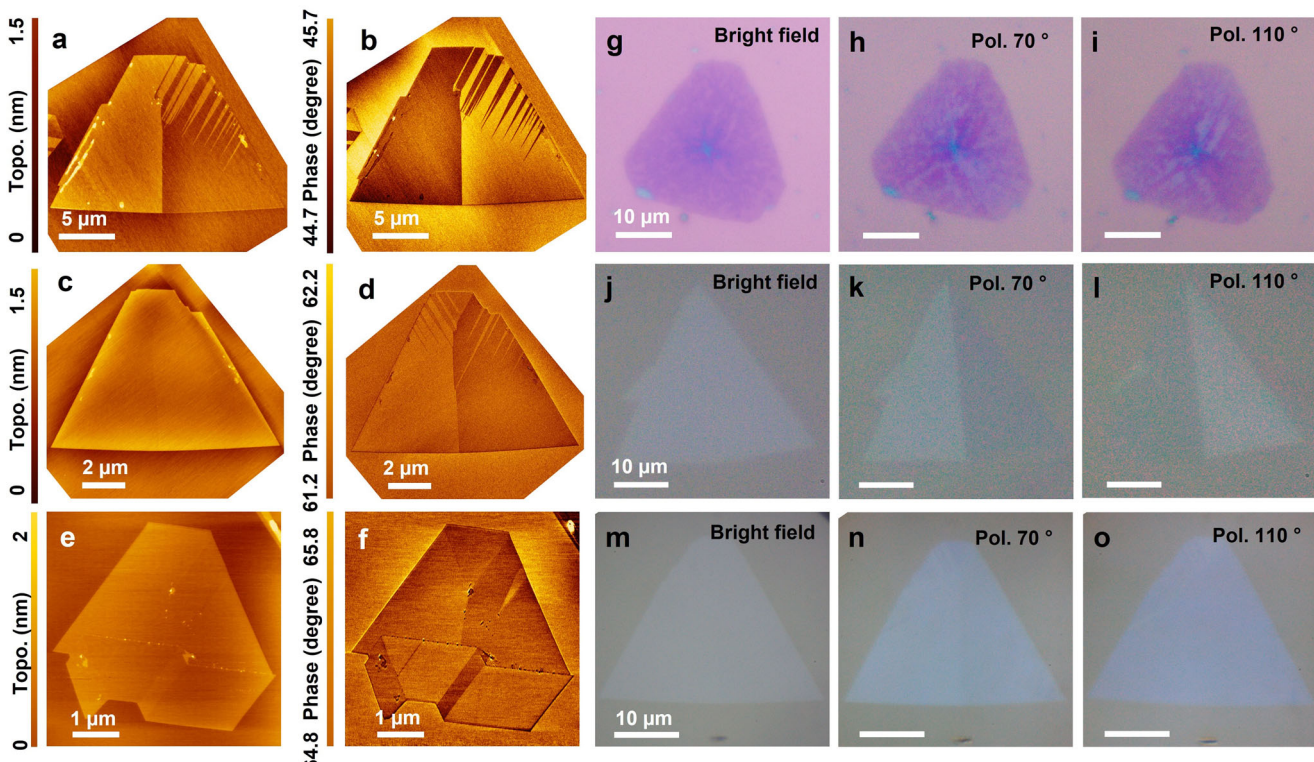
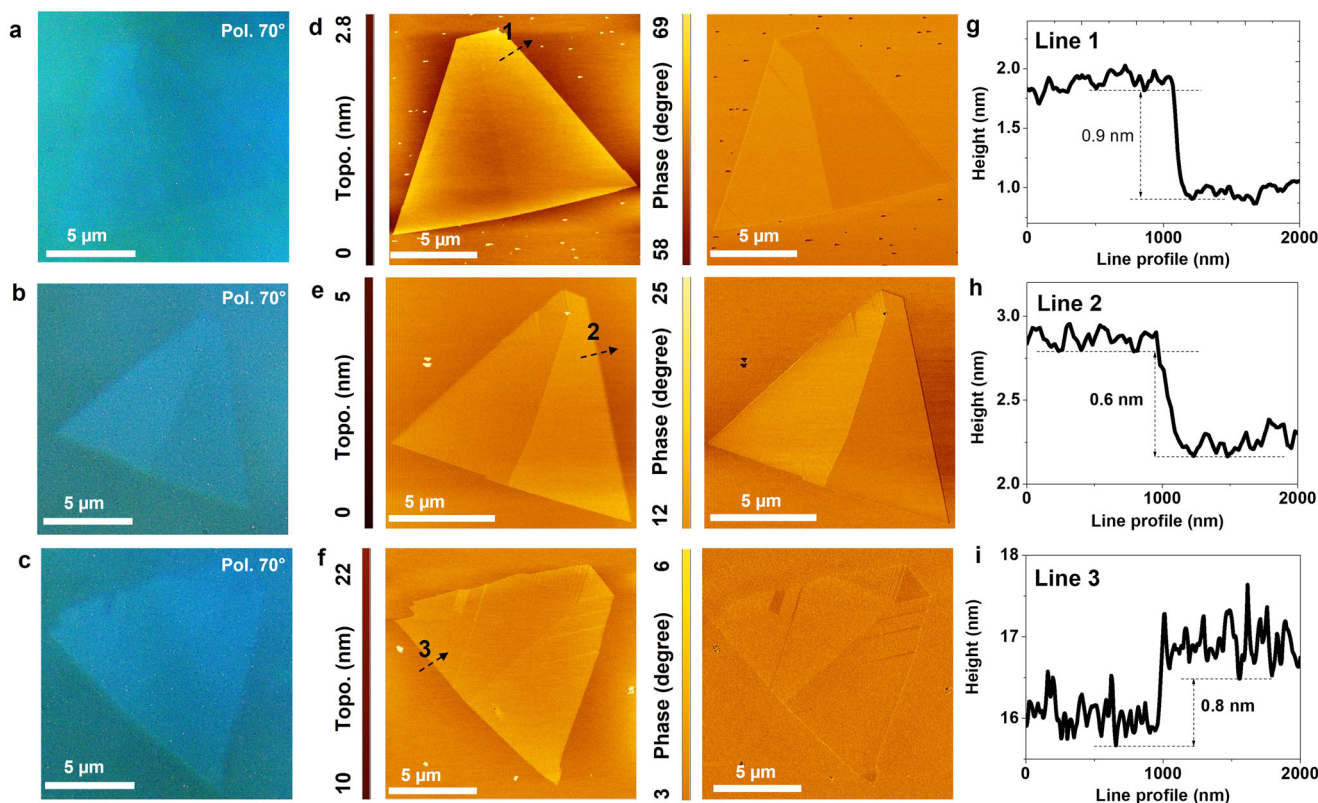


Fig. 4 Size dependence and substrate effects. **a, b** The DFM topography image and phase image of 20 μm 1L-ReS₂ grown on fluorophlogopite mica. **c, d** The DFM topography image and phase image of 10 μm 1L-ReS₂ grown on fluorophlogopite mica. **e, f** The DFM topography image and phase image of 5 μm 1L-ReS₂ grown on fluorophlogopite mica. **g-i, j-l, m-o** The optical micrographs of CVD-grown ReS₂ on 300 nm SiO₂/Si, c-face sapphire, and fluorophlogopite mica substrates, respectively.

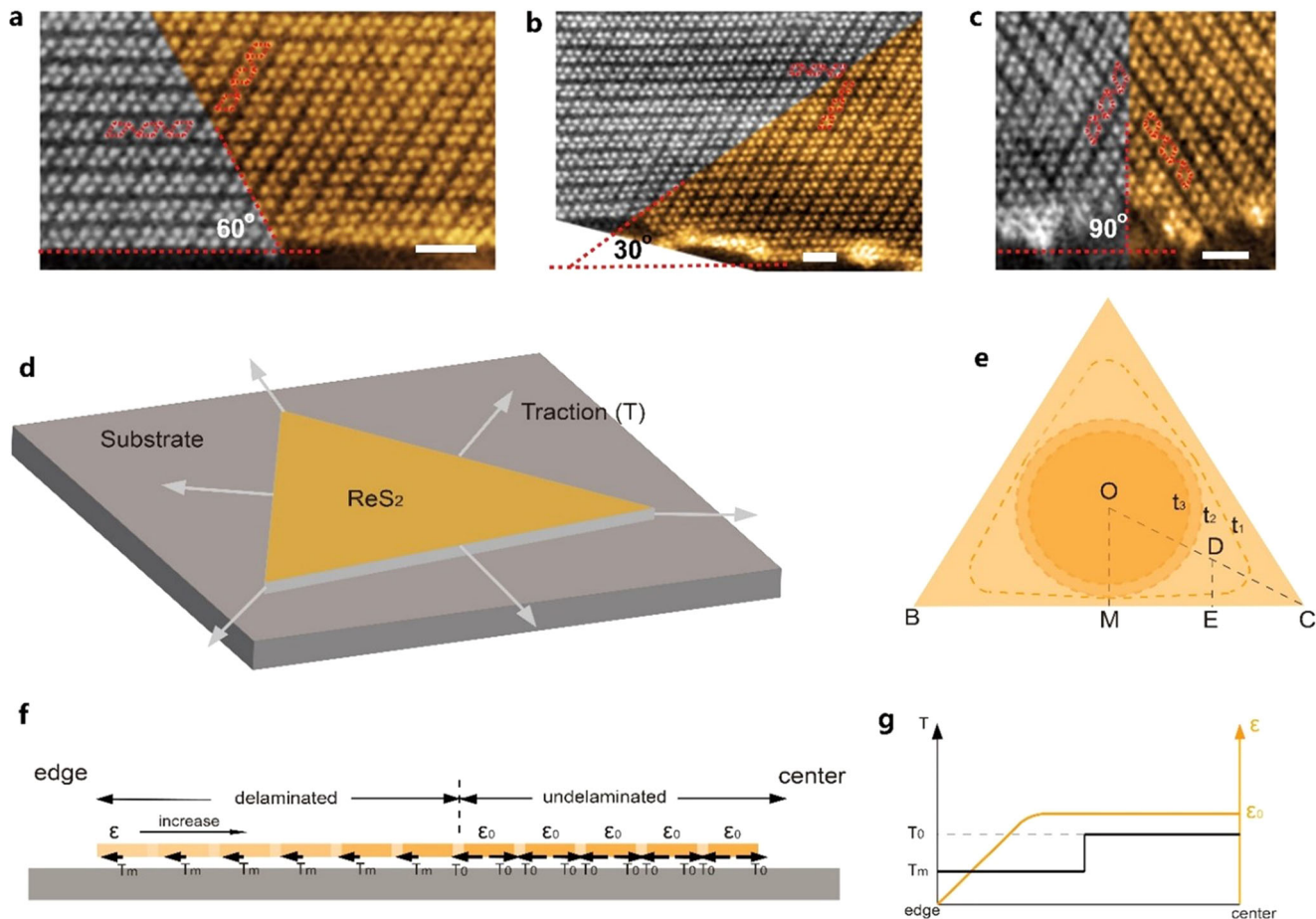


Fig. 5 The STEM images and illustration of strain field in ReS_2 . **a–c** The STEM annular dark field (ADF) images showing the typical twinning domain boundary structures stemming from free edges, the diamond chain directions (**b** direction in Fig. 6) are highlighted, scale bars =1 nm. **d** The tensile tractions on ReS_2 flake exerted by the engaged substrate. **e** The sketch map of the tensile strain level, decreasing from the center to flake edges. **f** The mechanical schematic of tensile strain resulted interfacial sliding and traction forces in equilibrium. **g** The diagram illustration traction and strain level associated with the location in the sample flakes.

structure or called T' (tetrahedral) phases^{39,45}. This structure is flexible to switch either two of the base vectors (**a, b, i**) under ultra-low straining (see Fig. 6a, b, and Supplementary Fig. 8), the 1L- ReS_2 structures are relaxed by density functional theory (DFT) calculations, see “Methods” section. We have listed all the possible normal strains and shear strains that can result in the lattice switching (viz. lattice reconstruction) in monolayer ReS_2 (Fig. 6c–n). For the three types of twin boundaries (Fig. 6c, d, e), the twin boundary directions are always in 0° or 60° with respect to the zigzag edges of 2D ReS_2 , while for the other three types of twin boundaries (Fig. 6i, j, k), the twin boundary directions are in 30° or 90° with respect to the zigzag edges of 2D ReS_2 . Therefore, we can readily distinguish these two groups of twin boundaries from the DFM or polarized OM images. It should be noted here that the strain condition needs to be comprehensively understood with the domain structures resulted from lattice reconstructions, and the strain effect for these lattice reconstructions are not relevant to the exact atomic structures of the domain boundaries, but only determined by the original (pristine) and the reconstructed domains. In principle, there is no strain along all the twinning domain boundaries. However, in other directions, the lattice reconstructions can accommodate the in-plane normal strain (either compressive or tensile) from -1.5% to 2.5% , and the in-plane shear strain (in terms of shear angle for certain directions) from -1.6° to 3.4° (Fig. 6c–n), depending on the

orientation of twin boundaries (along **a, b, i, u, v, w**, respectively, see Fig. 6a for the definition).

Apparently, the domain boundaries prefer to be twinning boundaries for the lowest energy cost (least lattice mismatch and zero strain along twin boundary directions). The remarkable low shear or normal strain (shear angle $<1\text{--}2^\circ$) that absorbed by twinning are associated with the lattice reconstruction in such anisotropic 2D materials. The parallel needle-like or stripe-like domain structures well resemble the famous martensite phases⁴⁶ widely existed, however, the energy required for twinning here are much lower than the normal mechanical twinning. Therefore, such lattice reconstruction can act as an efficient deformation mechanism for low straining level in 2D ReS_2 . Classified by boundary angles with respective to the ReS_2 edges, the triangular domain structures (twin boundary in 90° or 30° with edges) and the parallel stripe domains (twin boundary in 60° with edges) can be correlated with the deformation under shear and normal stress in samples, respectively (Fig. 6o, p). In addition, it should be noted that if the sulfur (S) atoms are considered, the lattice symmetry normal to the basal plane needs to be counted. That is, the S atoms cannot penetrate the basal plane during lattice reconstructions, so only the cases shown in Fig. 6c–e are entirely twin boundaries (for both Re and S atoms), whereas the cases in Fig. 6i–k are twin boundaries for Re atoms, but inverse twin boundaries for S atoms.

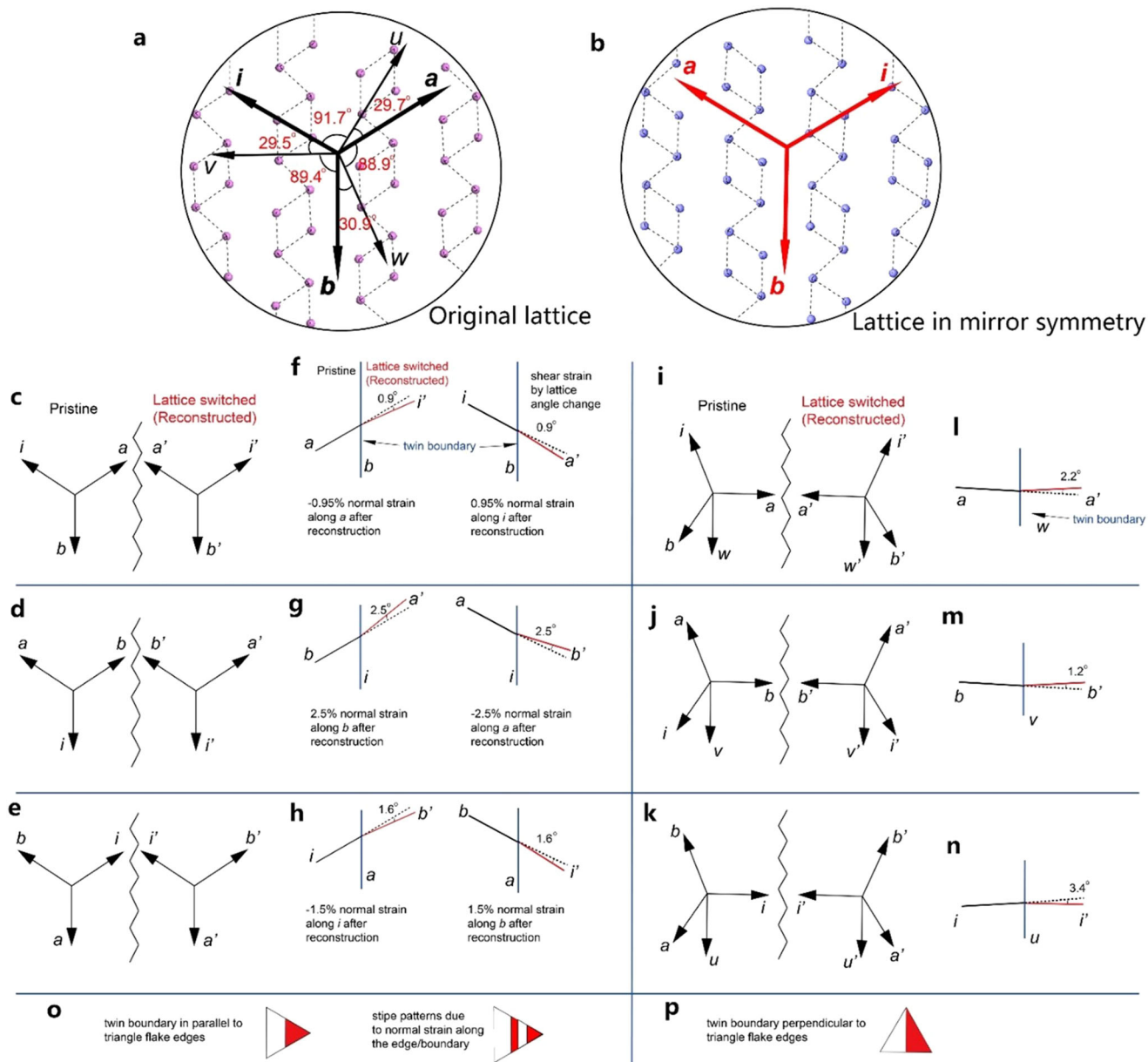


Fig. 6 The structural and strain analysis of twin structures by lattice reconstructions in 1L-ReS₂. **a** The original (pristine) lattice relaxed by DFT calculations. Specific vectors are defined for low-index crystal orientations (<100> and <110> directions), and only Re atoms shown. **b** The lattice in mirror symmetry to **a**. Lattice in **b** can be considered as after reconstruction from **a**. **c–e**, **i–k** Scheme of the twinning domain boundaries (zigzag lines) along different low-index orientations. Lattice orientations for two opposite sides of twin boundaries are shown by arrows. **f–h**, **l–n** The shear angle of labeled crystal directions and the normal strain (only **f–h**, normal strain for **l–n** is zero) for reconstructed lattices compared to pristine lattices, corresponding to the six types of twin boundaries above (**c–e**, **i–k**), respectively. **o**, **p** The domain types resulted from corresponding lattice reconstructions. Panel **o** corresponds to **c–e** type twin boundaries, while panel **p** corresponds to **i–k** type twin boundaries.

Next, opposite to the tensile strain discussed above, we will focus on the effects of compressive stress on the 2D anisotropic materials. The biaxial compressive strain in 2D materials can be generated by flexible substrates in the previous works⁴⁷. Albeit the wrinkle patterns can be frequently seen in 2D materials strained by the underlying flexible substrates^{48,49}, mechanical approach is less controllable, particularly for biaxial straining. Here we applied ultraviolet (UV) exposure with moisture condition on the 2D ReS₂ samples (see “Methods” section for details). Unlike the previous graphene or isotropic TMD materials^{50,51}, the regular wrinkle patterns emerged in 2D ReS₂. As seen from the DFM characterization results, the wrinkles preferentially follow the low-index directions (Fig. 7 and Supplementary Figs. 9,

10). The wavelengths, wrinkle heights for these three main directions are maintained almost identical throughout all the sub-domains in the flake (originated from CVD cooling) (Fig. 7e, f). Therefore, the wrinkle patterns also exhibit the domain patterns following the crystals. Apart from the preferences in crystal orientations, the wrinkles are prone to be formed along the domain boundaries. More wrinkle patterns generated can be found in Supplementary Fig. 10.

The compressive strain above is supplied by the photochemistry relevant to the surface of ReS₂ (see “Methods” section). The oxygen and hydroxyl radicals introduced by UV treatment are able to anchor in the lattice space lead to the compressive strain in the lattice. Supplementary Fig. 11a–c shows the TEM

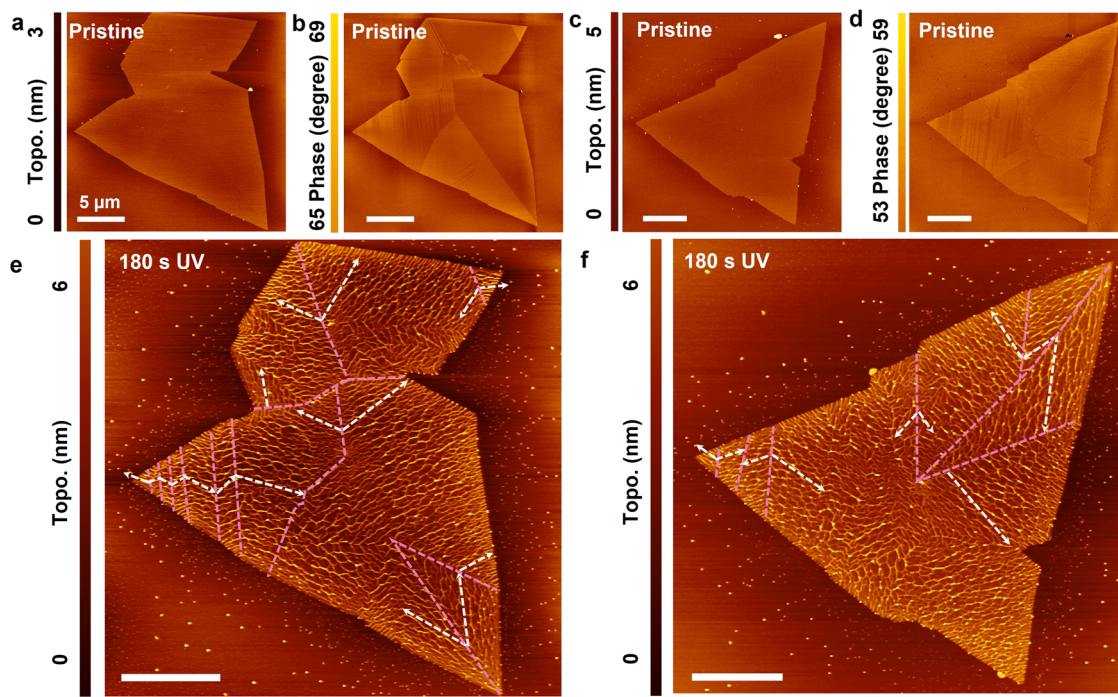


Fig. 7 The results of DFM characterizations and wrinkling behavior of 1L-ReS₂ as grown on fluorophlogopite mica substrate after 180 s UV treatment. **a-d** The DFM topography and phase images for pristine 1L-ReS₂. **e, f** The DFM images for 180 s UV treated ReS₂ flake in **a** and **c**, respectively. The white dashed lines with arrows indicate the different directional wrinkles and the sub-domain boundaries are marked by purple dashed lines.

characterization result of the spontaneous 2D wrinkling in monolayer ReS₂ under the biaxial compressive field. The wrinkles formation during UV treatment tends to follow the energy favorable directions—along basis vectors **a** or **b**. As shown in Supplementary Fig. 11d, the expansion of lattices after UV oxidation is confirmed by our DFT simulations. The basal plane is expanded during UV treatment meanwhile the ReS₂ are constrained by the underlying substrates, subsequently, the wrinkles can be developed to release the stress. The atomic structures of 1L-ReS₂ can be slightly distorted with the exotic covalently-bonded surface oxygen atoms⁴¹. The ReS₂ fold (Supplementary Fig. 11e) is also in part owing to the stacking of two counter layers after folding (the stable wrinkles can be reckoned as vertical folds)^{52,53}, along these directions has the lowest interlayer energies. It should also be noted that due to the monoclinic structure of 1L-ReS₂, the folded two layers (in mirror symmetry) cannot match each other (rotate by 1–2 degrees) with the original lattice. Therefore, to minimize the stacking energy of the wrinkles, lattice switching can take place and accommodate the strains (Supplementary Fig. 11f).

The wrinkles along the grain boundaries (by merging/stitching of grains during growth from different nuclei) (Fig. 7e, f) are also clearly observed. The wrinkle structures close to the edges are related to the special strain distribution along the edges (almost zero strain parallel to edges), hence the remaining compressive strain perpendicular to edges will generate the perfect periodic one-dimensional wrinkle patterns. Close to the edges, there are always less interactions from the substrate effects, rendering the wavelength/period of the wrinkles also become larger at edges (Supplementary Fig. 10).

According to the above experiments and explicit analysis, it has been clarified that the strain effects play essential roles in the formation of martensite-like structures and the twinning domain boundaries in anisotropic 2D materials such as ReS₂, and ReSe₂. These domain structures can conversely have a significant impact on the mechanical behavior as well as other physical properties.

The rich atomic structural reconstructions under strain loading, and the associated strong anisotropy in physical properties (electrical, electronic, optical, etc.), could open great opportunities for future strain engineering on these anisotropic 2D materials.

Methods

Synthesis of ReS₂ on fluorophlogopite mica, c-face sapphire and 300 nm SiO₂/Si, MoS₂ on 300 nm SiO₂/Si substrates. 1L-ReS₂ and MoS₂ flakes are synthesized in a two-splitting heating center tubular furnace. Firstly, 2 mg ammonium perrenhatte (NH₄ReO₄) (Aldrich, 99.999%) powder for ReS₂ growth, sodium molybdate dihydrate (Na₂MoO₄·2H₂O) (Aldrich, 99%) for MoS₂ growth is placed in a quartz boat and covered by a piece of 1 cm * 1 cm fluorophlogopite mica (KMg₃AlSi₃O₁₀F₂), c-face sapphire or 300 nm SiO₂/Si substrate then located on the downstream heating center. Next, 100 mg sulfur (Aldrich, 99.998%) plates for ReS₂ and MoS₂ growth are placed in a separated quartz boat located on the upstream heating center.

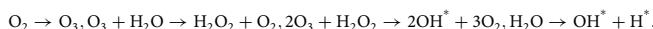
As the downstream heating center ramped up to 850 and 800 °C, for ReS₂ and MoS₂ growth, respectively. Meanwhile, the upstream heating center climbed to 200 °C. The 80 sccm Argon carrier gas is introduced during synthesis. After maintaining the target temperature for 10 min, the furnace is cooled down naturally.

Transfer of ReS₂ sample on SiO₂/Si, TEM grid. The as-grown ReS₂ was spin-coated with polymethyl methacrylate (PMMA) (A4) to form PMMA/ReS₂/substrate structure. Next, the PMMA/ReS₂/substrate is floated on the 75 °C ultrapure water for one hour to detach PMMA/ReS₂ from the substrate. Following, a 300 nm SiO₂/Si substrate or Quantifoil™ TEM grid is applied to scoop out the PMMA/ReS₂ film. Subsequently, the PMMA/ReS₂ on the target substrate was dried under ambient temperature to increase the adhesion between ReS₂ and the target substrate. Finally, the acetone or acetone vapor is introduced to remove the PMMA layer on 300 nm SiO₂/Si substrate or on the TEM grid, respectively.

Prepare of ReS₂ on SiO₂/Si from a bulk sample. With the assistance of the semiconductor transfer tape (USI, Blue Adhesive Plastic Film), bulk ReS₂ (2D Semiconductors Inc., USA) was exfoliated into pieces and attached to a 300 nm SiO₂/Si substrate.

UV treatment method. 1L-ReS₂ on the substrate is placed into a chamber fitted out a mercury lamp (LH-arc, Lichtzen Co. Ltd, Korea) with ~90% of emitted light at a wavelength of 254 nm and the minority of light at a wavelength of 185 nm (20 mW cm⁻²). The chamber is connected with two injection pipes and one output

valve. One injection pipe is for a humidifier to introduce moisture, while another one is for N₂ gas to extrude the humid and the output valve is used to balance the pressure at ambient pressure. The humid level was monitored using a hygrometer (accuracy $\pm 3\%$). The 1L-ReS₂ is treated with UV light for 180 s. The radicals were generated by UV light treated moisture air as the following reactions:



Angle-resolved polarized Raman (ARPR) measurement. The ARPR measurement is performed using a commercial inVia confocal Raman microscope (Renishaw, UK) with a $\times 50/0.75$ N.A. objective (LEICA, German) with a spatial resolution $\sim 1\text{ }\mu\text{m}$. The ARPR of ReS₂ and MoS₂ are measured at excitation wavelengths of 785 nm ($\sim 1.6\text{ mW}$ power) and 514 nm laser ($\sim 0.54\text{ mW}$ power) with 1200 l mm^{-1} grating and 1800 l mm^{-1} grating with a $\times 50/0.75$ N.A. objective (LEICA, German), respectively. The laser power is calibrated using standard photodiode power sensor S121C (Thorlabs, USA). The ARPR measurement setup is equipped with a rotatable Polarizer I, one half-wave plate, and a linear Polarizer II, the setup shown in Supplementary Fig. 4. The ARPR spectra are recorded every 10° with the incident laser being rotated by Polarizer I from 0° to 360° while the sample is fixed. As analyzer, the half-wave plate and the linear Polarizer II are applied to collect the scattered light. The ARPR spectra were fitted using Gaussian contributions to extract the peak intensity value.

DFM measurement. The topography and phase images are recorded using an AFM5300E system (HITACHI, Japan) in cyclic contact mode. The topography image and phase image are recorded through detection of the oscillation evolution of the cantilever. Initially, the cantilever oscillation is driven by the input signal. During the scanning, the force between the probe and the sample surface is maintained to be constant then the cantilever oscillation state changes. On the one hand, the topography images are generated by the amplitude evolution of the cantilever oscillation as shown in Supplementary Fig. 12a. On the other hand, the phase shift contrast is attributed to the energy adsorption of the sample surface, such as the delaminated area will have the less adsorptive energy, which results in a smaller phase shift (Supplementary Fig. 12b). The n-type silicon tip NSG30 (Tipsnano, Estonia) with Au coating on the reflective side is used for the measurement. The tip curvature radius is $\sim 35\text{ nm}$ with typical resonant frequency and force constant at 320 kHz and 40 N m^{-1} , respectively.

DFT calculations. Structure relaxations and energies of ReS₂ are calculated by using density functional theory as implemented in the Vienna ab initio simulation package (VASP)^{54,55} within the projector augmented wave (PAW)⁵⁶. The Perdew, Burke, and Ernzerhof (PBE) exchange-correlation functional⁵⁷ of the generalized gradient approximation (GGA)⁵⁸ is used to describe the electron interactions. A plane-wave cutoff energy of 450 eV is adopted for all the calculations. The vacuum space in z direction is set to be more than 15 \AA to prevent the interaction between layers. The criteria for convergence in energy is 10^{-5} eV . Structure relaxations and lattice constant are obtained by optimizing all atomic positions until the Hellmann-Feynman forces are less than 0.02 eV \AA^{-1} . The Brillouin zone is sampled with $8 \times 8 \times 1\text{ \Gamma}$ centered k points for structural optimizations.

Data availability

All data sets needed to evaluate the conclusions are presented in the paper. Additional data related to this paper may be requested from the authors for educational and academic purposes.

Received: 30 December 2020; Accepted: 21 July 2021;

Published online: 23 August 2021

References

- Lee, C., Wei, X. D., Kysar, J. W. & Hone, J. Measurement of the elastic properties and intrinsic strength of monolayer graphene. *Science* **321**, 385–388 (2008).
- Androulidakis, C., Koukaras, E. N., Paterakis, G., Trakakis, G. & Galiotis, C. Tunable macroscale structural superlubricity in two-layer graphene via strain engineering. *Nat. Commun.* **11**, 1–11 (2020).
- Qi, Y. et al. Superconductivity in Weyl semimetal candidate MoTe₂. *Nat. Commun.* **7**, 1–7 (2016).
- Zhang, X. et al. Two-dimensional MoS₂-enabled flexible rectenna for Wi-Fi band wireless energy harvesting. *Nature* **566**, 368–372 (2019).
- Lee, G. H. et al. High-strength chemical-vapor-deposited graphene and grain boundaries. *Science* **340**, 1073–1076 (2013).
- Liu, Z. et al. Strain and structure heterogeneity in MoS₂ atomic layers grown by chemical vapour deposition. *Nat. Commun.* **5**, 1–9 (2014).
- Ni, Z. H. et al. Uniaxial strain on graphene: Raman spectroscopy study and band-gap opening. *ACS Nano* **2**, 2301–2305 (2008).
- Lloyd, D. et al. Band gap engineering with ultralarge biaxial strains in suspended monolayer MoS₂. *Nano Lett.* **16**, 5836–5841 (2016).
- Shi, H. L., Pan, H., Zhang, Y. W. & Yakobson, B. I. Quasiparticle band structures and optical properties of strained monolayer MoS₂ and WS₂. *Phys. Rev. B* **87**, 155304 (2013).
- Ho, C. H. Optical study of the structural change in ReS₂ single crystals using polarized thermoreflectance spectroscopy. *Opt. Express* **13**, 8–19 (2005).
- Yu, S. et al. Strain-engineering the anisotropic electrical conductance in ReS₂ monolayer. *Appl. Phys. Lett.* **108**, 191901 (2016).
- Zhou, Z. et al. Anisotropic Raman scattering and mobility in monolayer 1T_d-ReS₂ controlled by strain engineering. *Appl. Surf. Sci.* **404**, 276–281 (2017).
- Li, J., Shan, Z. W. & Ma, E. Elastic strain engineering for unprecedented materials properties. *Mrs Bull* **39**, 108–117 (2014).
- Novoselov, K. S. et al. Two-dimensional atomic crystals. *Proc. Natl. Acad. Sci. USA* **102**, 10451–10453 (2005).
- Shin, B. G. et al. Indirect bandgap puddles in monolayer MoS₂ by substrate-induced local strain. *Adv. Mater.* **28**, 9378–9384 (2016).
- Bao, W. Z. et al. Controlled ripple texturing of suspended graphene and ultrathin graphite membranes. *Nat. Nanotechnol.* **4**, 562–566 (2009).
- Luo, S. et al. Formation of ripples in atomically thin MoS₂ and local strain engineering of electrostatic properties. *Nanotechnology* **26**, 105705 (2015).
- Cadelano, E., Palla, P. L., Giordano, S. & Colombo, L. Nonlinear elasticity of monolayer graphene. *Phys. Rev. Lett.* **102**, 235502 (2009).
- López-Polin, G. et al. Increasing the elastic modulus of graphene by controlled defect creation. *Nat. Phys.* **11**, 26–31 (2015).
- Li, T. S. Ideal strength and phonon instability in single-layer MoS₂. *Phys Rev B* **85**, 235407 (2012).
- Guinea, F., Katsnelson, M. I. & Vozmediano, M. A. H. Midgap states and charge inhomogeneities in corrugated graphene. *Phys. Rev. B* **77**, 075422 (2008).
- Yu, S. et al. Strain-engineering the anisotropic electrical conductance in ReS₂ monolayer. *Appl. Phys. Lett.* **108**, 191901 (2016).
- Singh, A. & Waghmare, U. V. Structural instabilities and wrinkles at the grain boundaries in 2-D h-BN: a first-principles analysis. *Phys. Chem. Chem. Phys.* **16**, 21664–21672 (2014).
- Li, Z. et al. Efficient strain modulation of 2D materials via polymer encapsulation. *Nat. Commun.* **11**, 1–8 (2020).
- Lee, J. E., Ahn, G., Shim, J., Lee, Y. S. & Ryu, S. Optical separation of mechanical strain from charge doping in graphene. *Nat. Commun.* **3**, 1–8 (2012).
- Lin, Y. C. et al. Single-layer ReS₂: two-dimensional semiconductor with tunable in-plane anisotropy. *ACS Nano* **9**, 11249–11257 (2015).
- Li, X. et al. Nanoassembly growth model for subdomain and grain boundary formation in 1T' layered ReS₂. *Adv. Funct. Mater.* **29**, 1906385 (2019).
- He, X. et al. Chemical vapor deposition of high-quality and atomically layered ReS₂. *Small* **11**, 5423–5429 (2015).
- Ho, C. H., Huang, Y. S., Tiong, K. K. & Liao, P. C. In-plane anisotropy of the optical and electrical properties of layered ReS₂ crystals. *J. Phys. Condens. Matter* **11**, 5367–5375 (1999).
- Zhong, H. X., Gao, S. Y., Shi, J. J. & Yang, L. Quasiparticle band gaps, excitonic effects, and anisotropic optical properties of the monolayer distorted 1T diamond-chain structures ReS₂ and ReSe₂. *Phys. Rev. B* **92**, 115438 (2015).
- Sim, S. et al. Selectively tunable optical stark effect of anisotropic excitons in atomically thin ReS₂. *Nat. Commun.* **7**, 1–6 (2016).
- Liu, E. et al. Integrated digital inverters based on two-dimensional anisotropic ReS₂ field-effect transistors. *Nat. Commun.* **6**, 1–7 (2015).
- Ovchinnikov, D. et al. Disorder engineering and conductivity dome in ReS₂ with electrolyte gating. *Nat. Commun.* **7**, 1–7 (2016).
- Wu, K. et al. Domain architectures and grain boundaries in chemical vapor deposited highly anisotropic ReS₂ monolayer films. *Nano Lett.* **16**, 5888–5894 (2016).
- Speer, J., Matlock, D. K., De Cooman, B. C. & Schroth, J. G. Carbon partitioning into austenite after martensite transformation. *Acta Mater.* **51**, 2611–2622 (2003).
- Kitahara, H., Ueji, R., Tsuji, N. & Minamino, Y. Crystallographic features of lath martensite in low-carbon steel. *Acta Mater.* **54**, 1274–1288 (2006).
- Li, X. et al. Controlled growth of large-area anisotropic ReS₂ atomic layer and its photodetector application. *Nanoscale* **8**, 18956–18962 (2016).
- Ottaviano, L. et al. Mechanical exfoliation and layer number identification of MoS₂ revisited. *2D Mater.* **4**, 045013 (2017).
- Hafeez, M., Gan, L., Li, H. Q., Ma, Y. & Zhai, T. Y. Chemical vapor deposition synthesis of ultrathin hexagonal ReS₂ flakes for anisotropic Raman property and optoelectronic application. *Adv. Mater.* **28**, 8296–8301 (2016).
- Tongay, S. et al. Monolayer behaviour in bulk ReS₂ due to electronic and vibrational decoupling. *Nat. Commun.* **5**, 1–6 (2014).

41. Huang, L. et al. Redox photochemistry on van der Waals surfaces for reversible doping in 2D materials. *Adv. Funct. Mater.* **14**, 2009166 (2021).
42. Yi, M. & Shen, Z. A review on mechanical exfoliation for the scalable production of graphene. *J. Mater. Chem. A* **3**, 11700–11715 (2015).
43. Yang, J. et al. Elastic and electronic tuning of magnetoresistance in MoTe₂. *Sci. Adv.* **3**, eaao4949 (2017).
44. Ly, T. H., Yun, S. J., Thi, Q. H. & Zhao, J. Edge delamination of monolayer transition metal dichalcogenides. *ACS Nano* **11**, 7534–7541 (2017).
45. Kertesz, M. & Hoffmann, R. Octahedral vs. trigonal-prismatic coordination and clustering in transition-metal dichalcogenides. *J. Am. Chem. Soc.* **106**, 3453–3460 (1984).
46. Calcagnotto, M., Ponge, D., Demir, E. & Raabe, D. Orientation gradients and geometrically necessary dislocations in ultrafine grained dual-phase steels studied by 2D and 3D EBSD. *Mater. Sci. Eng. A* **527**, 2738–2746 (2010).
47. Zhu, C. R. et al. Strain tuning of optical emission energy and polarization in monolayer and bilayer MoS₂. *Phys. Rev. B* **88**, 121301 (2013).
48. Tweedie, M. E. P. et al. Inhomogeneous strain release during bending of WS₂ on flexible substrates. *ACS Appl. Mater. Inter.* **10**, 39177–39186 (2018).
49. Brennan, C. J., Nguyen, J., Yu, E. T. & Lu, N. Interface adhesion between 2D Materials and elastomers measured by buckle delaminations. *Adv. Mater. Interfaces* **2**, 1500176 (2015).
50. Zhu, W. et al. Structure and electronic transport in graphene wrinkles. *Nano Lett.* **12**, 3431–3436 (2012).
51. Zhang, Q. et al. Strain relaxation of monolayer WS₂ on plastic substrate. *Adv. Funct. Mater.* **26**, 8707–8714 (2016).
52. Zheng, F. et al. The critical stable length in wrinkles of two-dimensional materials. *ACS Nano* **14**, 2137–2144 (2020).
53. Zhao, J. et al. Two-dimensional membrane as elastic shell with proof on the folds revealed by three-dimensional atomic mapping. *Nat. Commun.* **6**, 1–6 (2015).
54. Kresse, G. & Furthmüller, J. Efficient iterative schemes for ab initio total-energy calculations using a plane-wave basis set. *Phys. Rev. B* **54**, 11169 (1996).
55. Kresse, G. & Furthmüller, J. Efficiency of ab-initio total energy calculations for metals and semiconductors using a plane-wave basis set. *Comput. Mater. Sci.* **6**, 15–50 (1996).
56. Blöchl, P. E. Projector augmented-wave method. *Phys. Rev. B* **50**, 17953 (1994).
57. Perdew, J. P., Ernzerhof, M. & Burke, K. Rationale for mixing exact exchange with density functional approximations. *J. Chem. Phys.* **105**, 9982–9985 (1996).
58. Perdew, J. P., Burke, K. & Ernzerhof, M. Generalized gradient approximation made simple. *Phys. Rev. Lett.* **77**, 3865–3868 (1996).

Acknowledgements

This work was supported by the National Science Foundation of China (Project Nos. 51872248, 21703076, 51922113), the Hong Kong Research Grant Council under Early Career Scheme (Project Nos. 21303218, 25301018), and the Hong Kong Research Grant Council General Research Fund (Project Nos. 15302419, 11300820), City University of

Hong Kong (Project Nos. 9610387, 7005259), and Natural Science Foundation of Jiangsu Province of China (Project No. BK202100XX), Natural Science Foundation of the Jiangsu Higher Education Institutions of China (No. 18KJA140001), Shenzhen Science and Technology Innovation Commission (Project No. JCYJ20200109110213442), the Hong Kong Polytechnic University (Project Nos. ZVRP and ZVGH). We thank Mr. Tak Wai Wong for his help with the preparation of the experiment.

Author contributions

All authors were involved in data interpretation and manuscript preparation. L.H., F.Z., and H.C. conducted the experiments, performed the formal analysis, and original manuscript writing. Q.H.T., X.C., and H.L. performed the materials synthesis and characterizations. C.-S.L. consultation. T.H.L., J.Z., and Q.D. supervised the project, manuscript edit, and funding acquisition.

Competing interests

The authors declare no competing interests.

Additional information

Supplementary information The online version contains supplementary material available at <https://doi.org/10.1038/s43246-021-00190-7>.

Correspondence and requests for materials should be addressed to Q.D., J.Z. or T.H.L.

Peer review information *Communications Materials* thanks the anonymous reviewers for their contribution to the peer review of this work. Primary Handling Editor: John Plummer.

Reprints and permission information is available at <http://www.nature.com/reprints>

Publisher's note Springer Nature remains neutral with regard to jurisdictional claims in published maps and institutional affiliations.



Open Access This article is licensed under a Creative Commons Attribution 4.0 International License, which permits use, sharing, adaptation, distribution and reproduction in any medium or format, as long as you give appropriate credit to the original author(s) and the source, provide a link to the Creative Commons license, and indicate if changes were made. The images or other third party material in this article are included in the article's Creative Commons license, unless indicated otherwise in a credit line to the material. If material is not included in the article's Creative Commons license and your intended use is not permitted by statutory regulation or exceeds the permitted use, you will need to obtain permission directly from the copyright holder. To view a copy of this license, visit <http://creativecommons.org/licenses/by/4.0/>.

© The Author(s) 2021